Supplement of Atmos. Meas. Tech., 19, 1059–1076, 2026
https://doi.org/10.5194/amt-19-1059-2026-supplement

Atmospheric Measurement Techniques
Open Access
EGU

Supplement of

Improved estimation of diurnal variations in near-global PBLH through a hybrid WCT and transfer learning approach

Yarong Li et al.

Correspondence to: Jianjun He (hejianjun@cma.gov.cn)

Table S1. Accuracy (%) and MAE (m) for the first five peaks with different dilation factors range from 240 to 960 m.

	Dialation (m)	240	360	480	600	720	840	960
Accuracy (%)	First Peak	29.67	32.57	35.77	37.8	38.77	39.18	38.41
	Second Peak	17.58	17.21	17.07	16.16	16.92	16.72	15.65
	Third Peak	13.87	14.23	13.62	13.31	13.01	12.25	10.11
	Fourth Peak	14.68	12.91	11.16	12.04	9.1	4.27	0.56
	Fifth Peak	12.65	11.89	12.55	6.55	1.37	0	0
	Total	88.45	88.81	90.17	85.86	79.17	72.42	64.73
MAB (m)	First Peak	201.1	212.6	225.8	240.9	255.6	271.3	278.6
	Second Peak	225.2	245.8	255.0	271.5	280.8	298.6	300.2
	Third Peak	224.8	215.5	233.8	252.9	294.9	300.5	305.6
	Fourth Peak	214.9	225.0	232.0	248.7	244.3	250.4	236.8
	Fifth Peak	212.3	220.7	241.4	217.1	289.7	-	-

Table S2. Hit rate (%) of the first five peaks when setting different threshold for calculating accuracy.

Threshold (m)	300	400	500	600	700
First Peak	30.39	33.59	35.77	36.99	38.11
Second Peak	13.31	15.8	16.97	17.78	18.19
Third Peak	11.38	12.65	13.62	14.23	14.63
Fourth Peak	10.26	11.38	12.55	12.75	13.06
Fifth Peak	8.74	9.6	10.16	10.57	10.87

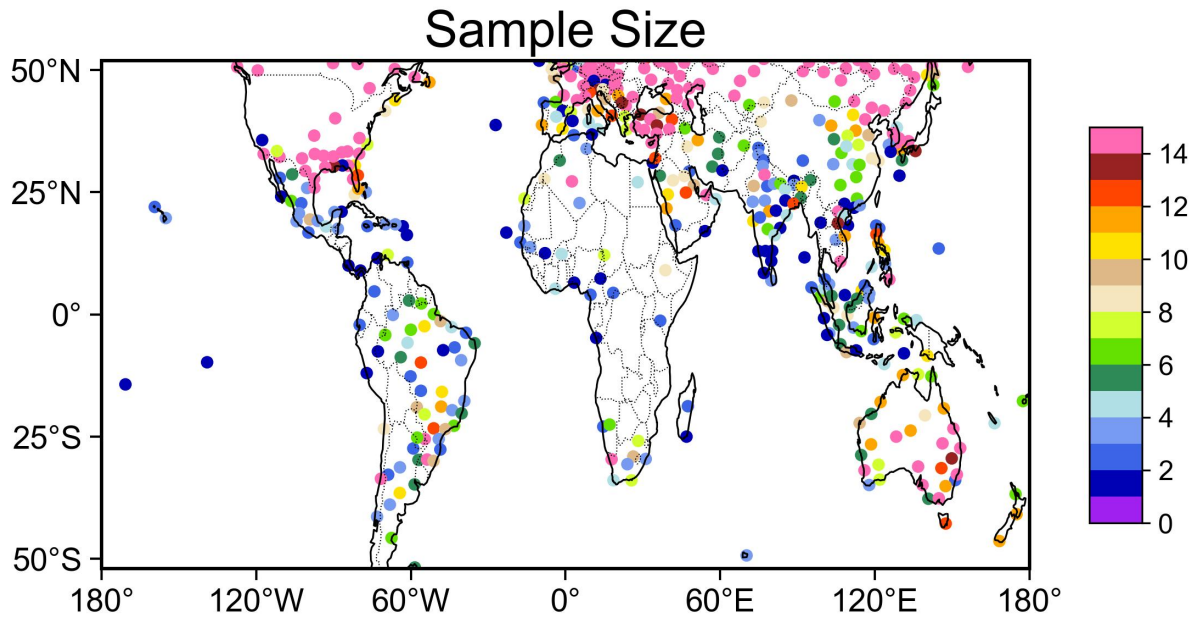

Fig. S1. Numbers of matched samples between CATS orbits and radiosonde sites.

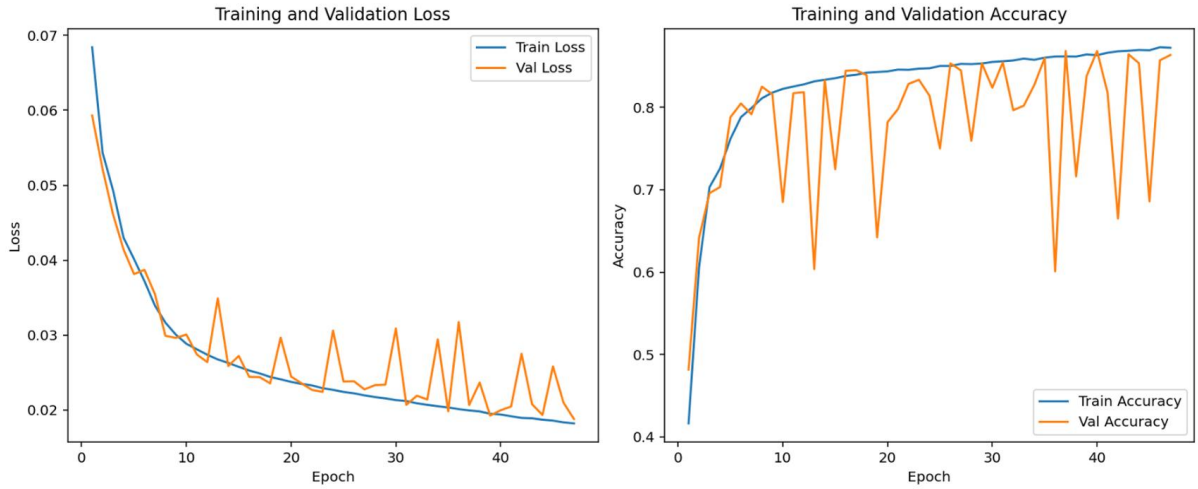

Fig. S2. Training curves for pre-trained model.

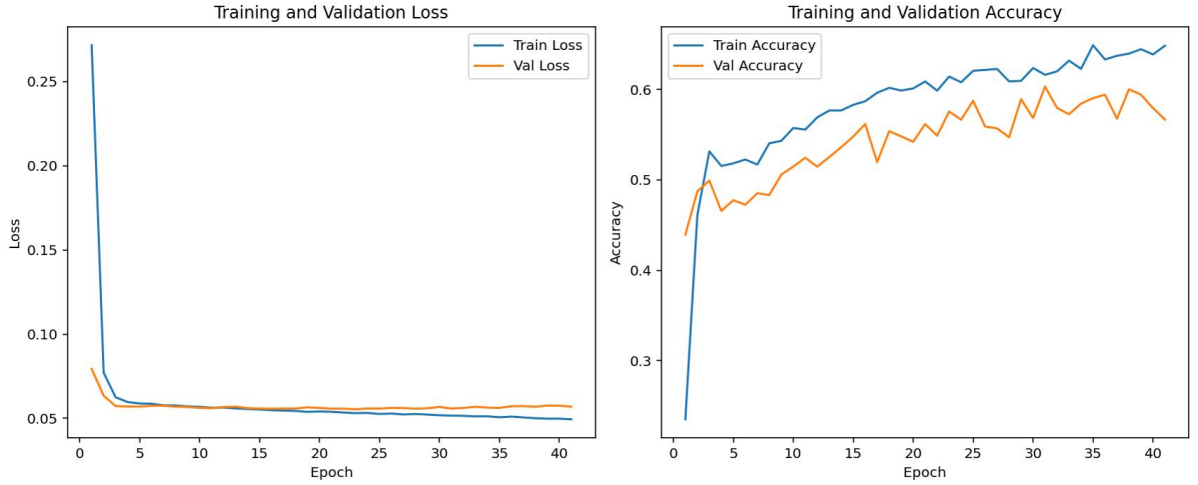

Fig. S3. Same as Fig. S2, but for training curves of base model, which is trained based on the dataset with target labels constrained by only radiosonde.

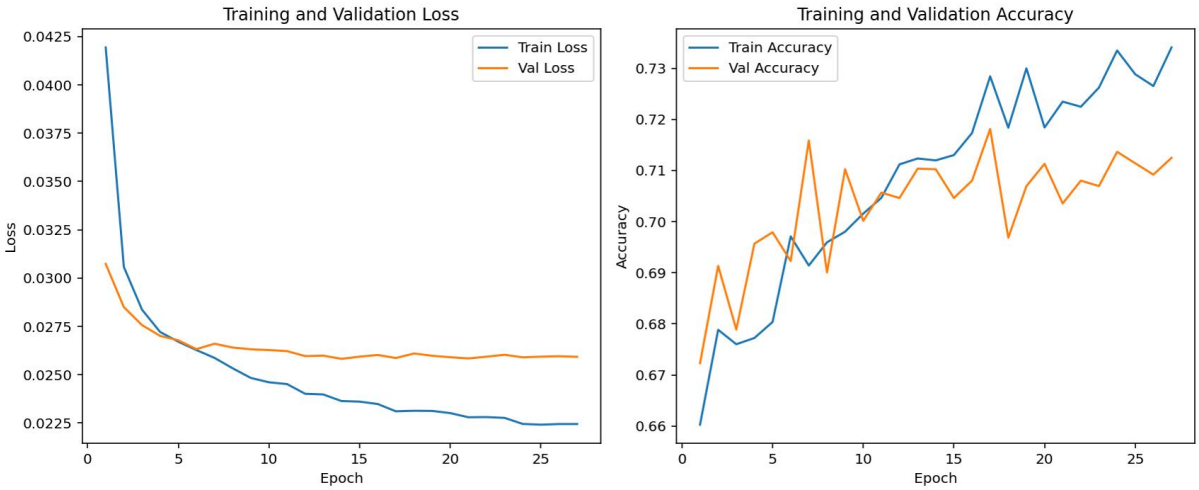

Fig. S4. Same as Fig. S2, but for curves when training the transfer model.

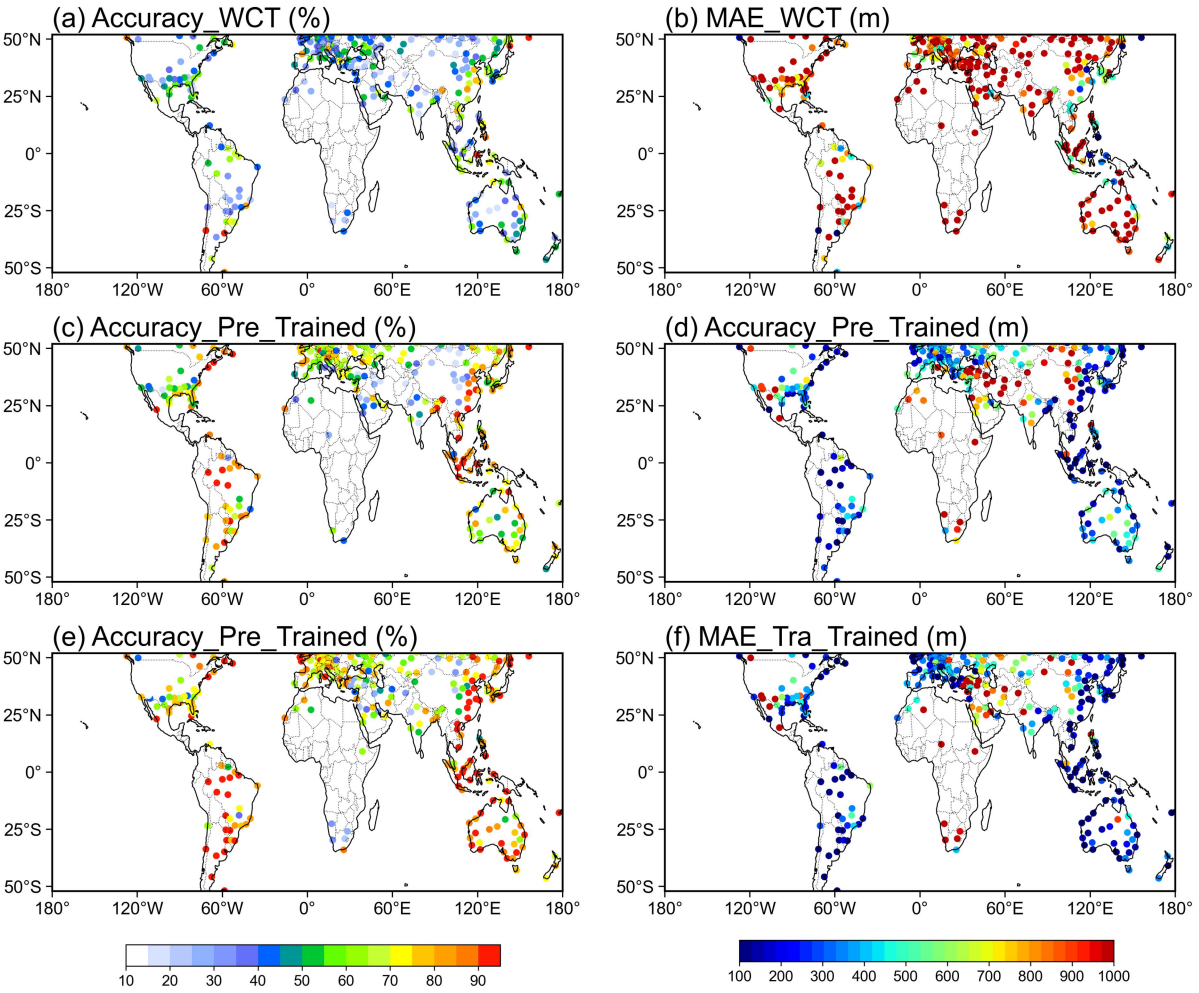

Fig. S5. Accuracy and MAE of the WCT (a-b), pre-train model (c-d), transfer model (e-f) when comparing against the radiosonde constrained PBLH labels.

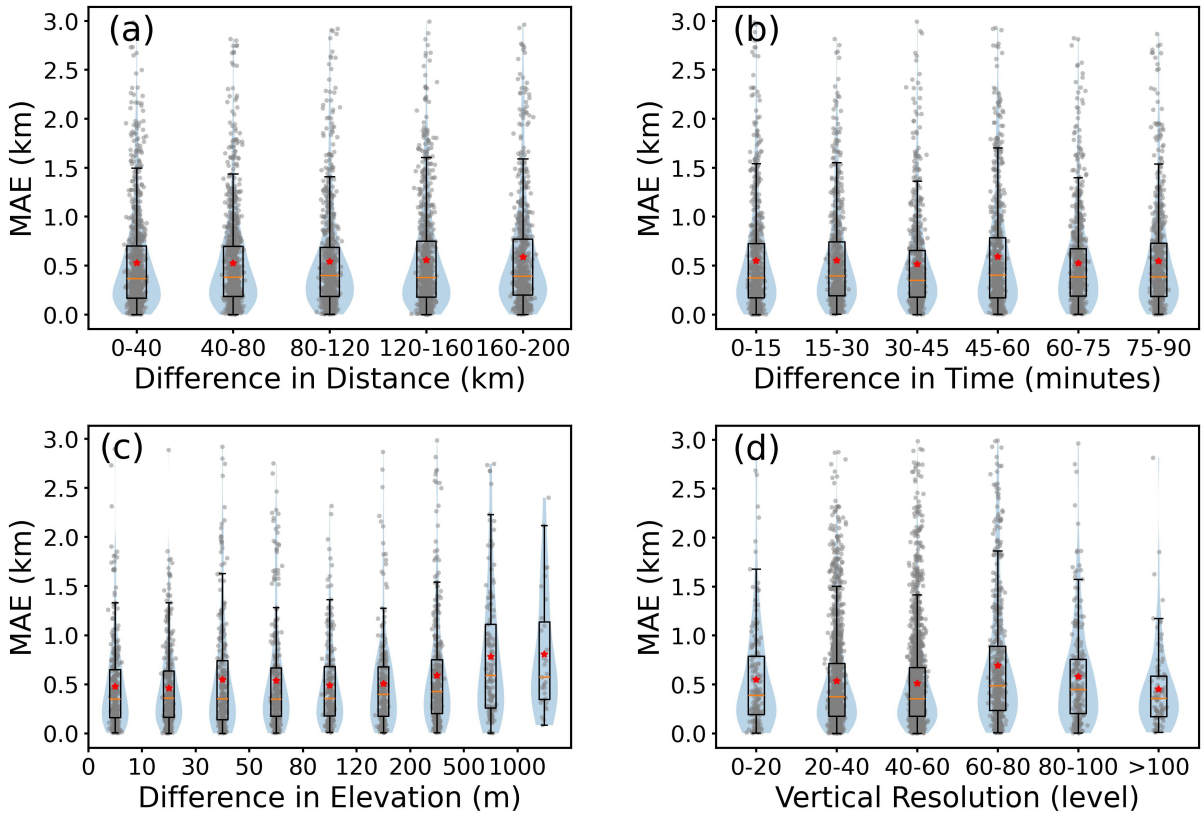

Fig. S6. Dependence of PBLH differences between the WCT and radiosonde on differences in distance (a), time (b), elevation (c), and vertical resolution of radiosonde (d).

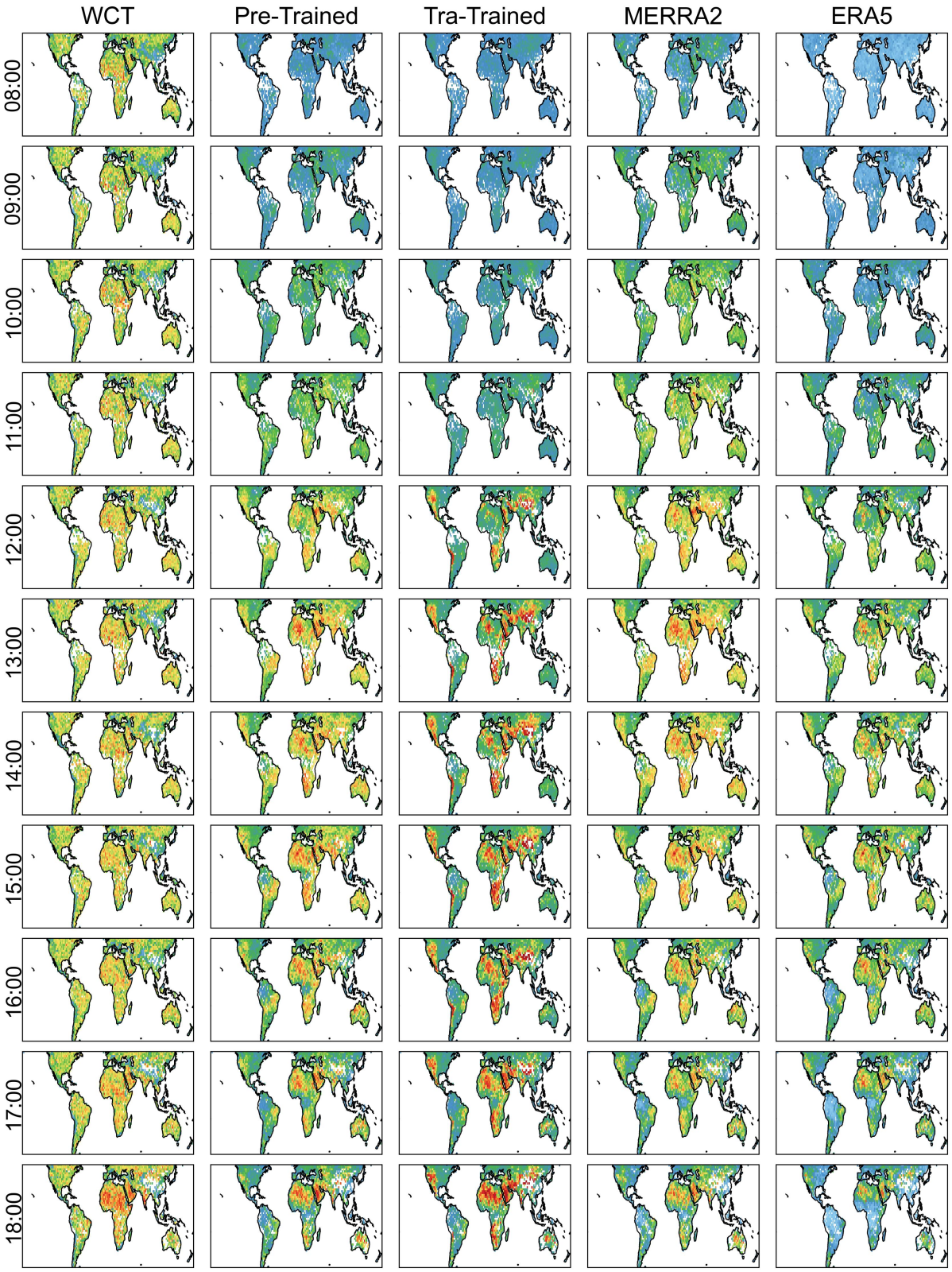

Fig. S7. Spatial distribution of hourly PBLH derived from the WCT, pre-trained model, transfer model, MERRA2, and ERA5 at each daily hour.

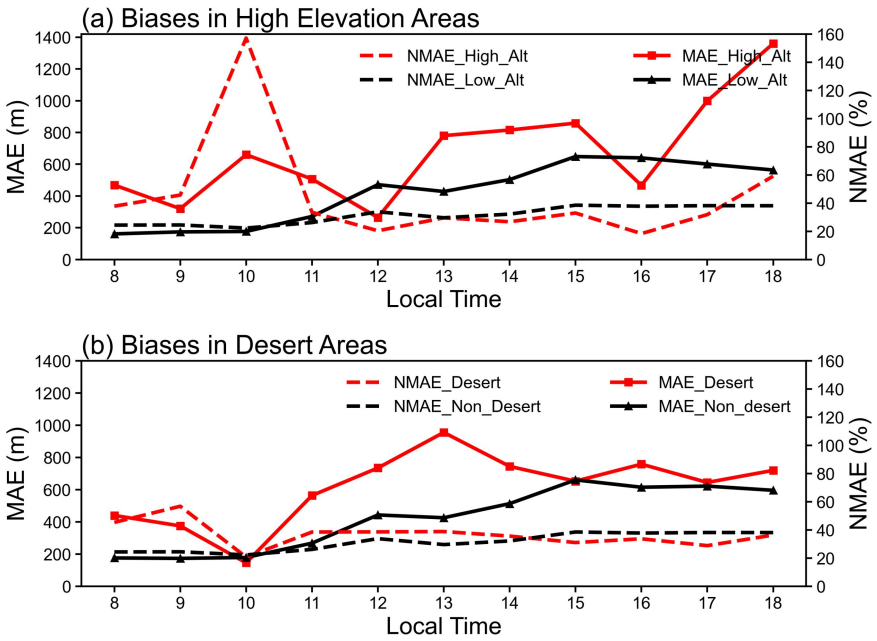

Fig. S8. Comparisons for MAE and NMAE of PBLH between high-altitude and low-altitude (a), and between deserts and non-deserts (b) at each daytime hour.

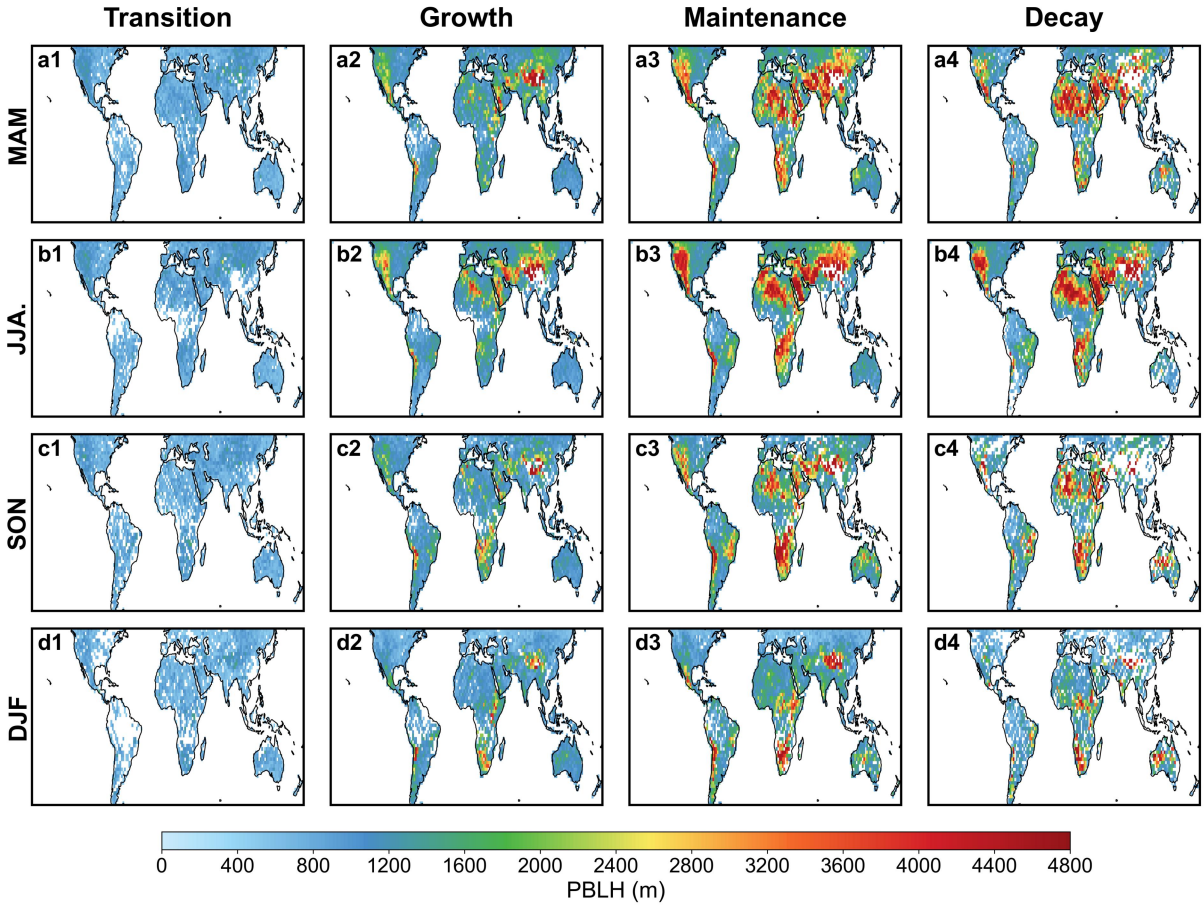

Fig. S9. Four evolution stages of PBLH derived from transfer model on the seasonal scale.

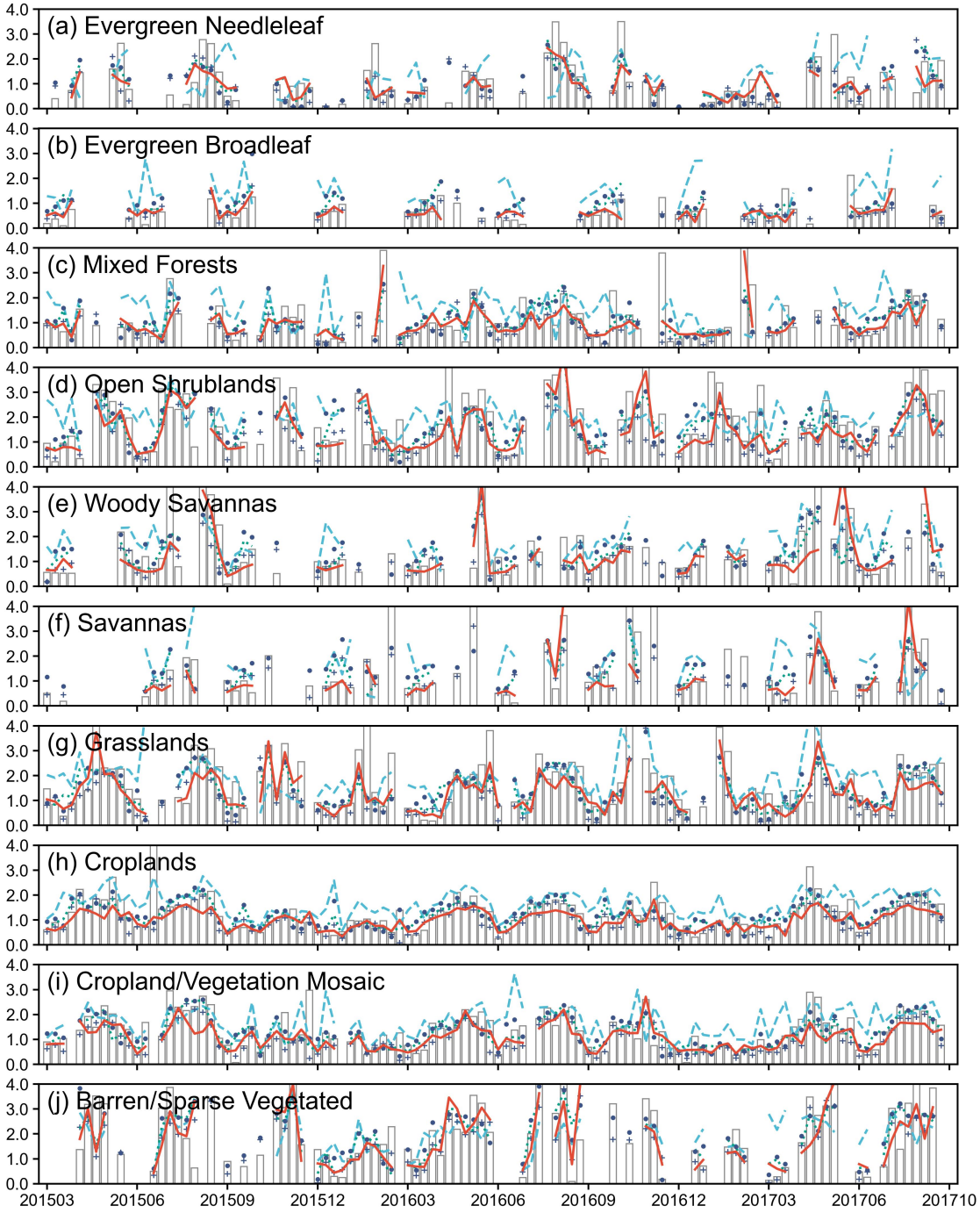

Fig. S10. Seasonally diurnal variations of PBLH on ten major land cover types, which are derived from radiosondes (columns), pre-train model (cyan dashed), transfer model (red solid), ERA5 (solid circle), and MERRA2 ('+').

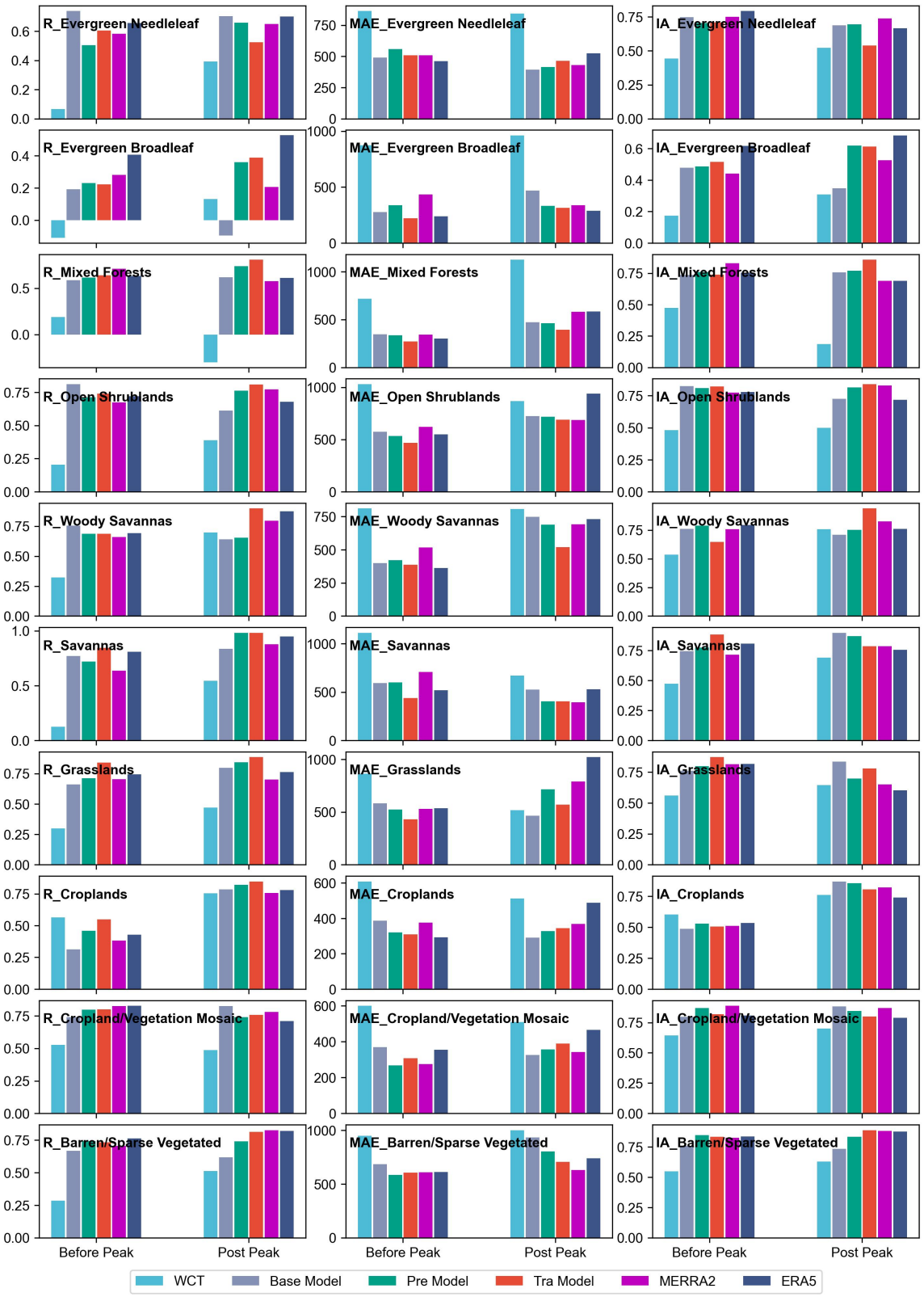

Fig. S11. R, MAE, and IA (index of agreement) between model/reanalysis predicted and radiosonde derived PBLH on ten major land cover types.